

THE CONSTANT AVERAGE RELATIONSHIP BETWEEN DUST-OBSCURED STAR FORMATION AND STELLAR MASS FROM $Z = 0$ TO $Z = 2.5$

KATHERINE E. WHITAKER^{1,2,6}, ALEXANDRA POPE², RYAN CYBULSKI³, CAITLIN M. CASEY⁴, GERGÖ POPPING⁵, MIN S. YUN²

Accepted for publication in the Astrophysical Journal

ABSTRACT

The total star formation budget of galaxies consists of the sum of the unobscured star formation, as observed in the rest-frame ultraviolet (UV), together with the obscured component that is absorbed and re-radiated by dust grains in the infrared. We explore how the fraction of obscured star formation depends on stellar mass for mass-complete samples of galaxies at $0 < z < 2.5$. We combine GALEX and WISE photometry for SDSS-selected galaxies with the 3D-HST treasury program and Spitzer/MIPS $24\mu\text{m}$ photometry in the well-studied 5 extragalactic CANDELS fields. We find a strong dependence of the fraction of obscured star formation ($f_{\text{obscured}} = \text{SFR}_{\text{IR}} / \text{SFR}_{\text{UV+IR}}$) on stellar mass, with remarkably little evolution in this fraction with redshift out to $z=2.5$. 50% of star formation is obscured for galaxies with $\log(M/M_{\odot})=9.4$; although unobscured star formation dominates the budget at lower masses, there exists a tail of low mass extremely obscured star-forming galaxies at $z > 1$. For $\log(M/M_{\odot}) > 10.5$, $>90\%$ of star formation is obscured at all redshifts. We also show that at fixed total SFR, f_{obscured} is lower at higher redshift. At fixed mass, high-redshift galaxies are observed to have more compact sizes and much higher star formation rates, gas fractions and hence surface densities (implying higher dust obscuration), yet we observe no redshift evolution in f_{obscured} with stellar mass. This poses a challenge to theoretical models to reproduce, where the observed compact sizes at high redshift seem in tension with lower dust obscuration.

Subject headings: galaxies: evolution — galaxies: formation — galaxies: high-redshift — dust, extinction

1. INTRODUCTION

The current census of the peak epoch of star formation, $z \sim 1 - 3$, reveals that the most massive galaxies are enshrouded in dust (e.g., Magnelli et al. 2009; Murphy et al. 2011; Bourne et al. 2017). These dust grains form a cocoon around nascent stars still embedded in their native birth sites, preferentially absorbing the ultraviolet (UV) stellar radiation and thermally re-radiating in the far-infrared (FIR) (Seibert et al. 2005; Cortese et al. 2006; Muñoz-Mateos et al. 2009). It is this interstellar dust extinction that introduces the largest source of systematic error into global measurements of the star formation rates (SFR) of galaxies (Kennicutt 1998a).

There are several standard methods employed to account for dust attenuation to attain a complete view of star formation. The unobscured star formation measured from the non-ionizing rest-frame UV continuum ($\sim 130\text{--}250\text{nm}$) of massive recently formed stars can be corrected using empirical calibrations based on the UV slope from the spectral energy distributions (e.g., Meurer et al. 1999). However, these calibrations are uncertain due to

potential intrinsic variations in the UV slope and dust attenuation curves (e.g., Battisti et al. 2016; Salmon et al. 2016). Alternatively, optical emission line diagnostics such as H α can be dust-corrected from the Balmer decrement (Kennicutt et al. 2009). But such observations are difficult to obtain across cosmic time and observationally expensive. One can also estimate total SFRs by directly measuring the obscured SFR_{IR} from one or more components of the mid- to FIR emission and co-adding this with the unobscured UV SFR. Although systematic uncertainties remain in calibrating the IR luminosity (Calzetti 2013), the main bottleneck has been in measuring accurate FIR emission for representative samples of star-forming galaxies across cosmic history.

Due to the onset of source confusion, the deepest attainable FIR and sub-millimeter (sub-mm) surveys to date are only sensitive to the most extreme galaxies (Casey et al. 2014a, and references therein). FIR and sub-mm selected galaxies are rare by number and likely do not represent the overall star-forming galaxy population. Given these current limitations, empirical calibrations of deep *Spitzer*/MIPS and *Herschel* stacks have instead been used to push the measurements of the average correlation between SFR and M_{\star} down to the equivalent M_{\star} limits of the *Hubble Space Telescope* (*HST*) legacy surveys (Viero et al. 2013; Whitaker et al. 2014). Although the majority of star formation is assumed to be unobscured in low-mass galaxies, the dust corrections are not insignificant. The goal of this paper is to quantify the level of obscured star formation as a function of M_{\star} and total SFR for mass-complete samples of galaxies across 80% of cosmic history (out to $z=2.5$). We will address the following questions: (1) how does the fraction

kwhitaker@astro.umass.edu

¹Department of Physics, University of Connecticut, Storrs, CT 06269, USA

²Department of Astronomy, University of Massachusetts, Amherst, MA 01003, USA

³Department of Physics and Astronomy, Tufts University, Medford, MA 02155, USA

⁴Department of Astronomy, The University of Texas at Austin, Austin, TX 78712, USA

⁵European Southern Observatory, Karl-Schwarzschild-Strasse 2, D-85748, Garching, Germany

⁶Hubble Fellow

of obscured star formation depend on M_* (Section 3.1)?, and (2) how does the fraction of obscured star formation depend on total SFR (Section 3.2)? In Section 4, we discuss the redshift evolution of these relations in the context of our current understanding of galaxy scaling relations and theoretical models. The conclusions of this paper are summarized in Section 5.

In this paper, we use a Chabrier (2003) initial mass function (IMF) and assume a Λ CDM cosmology with $\Omega_M = 0.3$, $\Omega_\Lambda = 0.7$, and $H_0 = 70 \text{ km s}^{-1} \text{ Mpc}^{-1}$.

2. DATA AND SAMPLE SELECTION

2.1. Stellar Masses, Redshifts and Rest-frame Colors

We use the multi-wavelength datasets of five well-studied extragalactic fields (AEGIS, COSMOS, GOODS-N, GOODS-S, and UDS) through the Cosmic Assembly Near-IR Deep Extragalactic Legacy Survey (CANDELS; Grogin et al. 2011) and the 3D-HST survey (Momcheva et al. 2016). With M_* , redshifts, and rest-frame colors from the 3D-HST 0.3–8 μm photometric (Skelton et al. 2014) and spectroscopic (Momcheva et al. 2016) catalogs, we leverage the analysis of the mass-complete sample of 39,106 star-forming galaxies at $0.5 < z < 2.5$ presented in Whitaker et al. (2014). The Skelton et al. (2014) photometric catalogs include a large compilation of optical to near-infrared (NIR) photometric broadband and medium-bandwidth filters, ranging from 18 filters in UDS up to 44 in COSMOS. Galaxies are identified using Source Extractor (Bertin & Arnouts 1996) with deep $J_{F125W} + H_{F140W} + H_{F160W}$ detection images. Redshifts and rest-frame colors are determined with the EAZY code (Brammer et al. 2008). Where possible, we combine the photometry with the spatially resolved low-resolution HST/WFC3 G141 grism spectroscopy to derive improved redshifts. The “best” redshift was rank ordered to be spectroscopic (4% total sample, 13% of galaxies with $\log(M_*/M_\odot) > 10$), grism (12% total, 38% massive), or photometric (84% total, 49% massive), depending on the availability. Star-forming galaxies are identified from rest-frame U-V and V-J colors following Whitaker et al. (2012a). Luminous active galactic nuclei are identified and removed using the *Spitzer*/IRAC color selections of Donley et al. (2012) due to its potential contamination of SFR_{IR} .

Stellar masses M_* are derived by fixing the redshift to “best”, as described above, and fitting stellar population synthesis templates with the FAST code (Kriek et al. 2009). The FAST templates include a grid of Bruzual & Charlot (2003) models that assume a Chabrier (2003) IMF with solar metallicity and a range of ages (7.6–10.1 Gyr), exponentially declining star formation histories ($7 < \tau < 10$ in log years) and dust extinction ($0 < A_V < 4$). The dust content is parameterized by the attenuation in the V-band following the Calzetti et al. (2000) extinction law. M_* is corrected for emission-line contamination of the broadband fluxes using values presented in Appendix A of Whitaker et al. (2014). The mass completeness limits employed herein correspond to the 90% completeness limits derived by Tal et al. (2014), calculated by comparing object detection in the CANDELS/deep with a re-combined subset of the exposures that reach the depth of the CANDELS/wide fields. Although the mass completeness in

the deeper GOODS-N and GOODS-S fields will extend to lower stellar masses, we adopt the more conservative limits for the shallower HST/WFC3 imaging. The resulting sample is mass-complete down to $\log(M/M_\odot) = 8.7$ (9.3) at $z = 1.0$ ($z = 2.5$).

2.2. Star Formation Rates

SFR_{IR} originates from stacking analyses in Whitaker et al. (2014), using *Spitzer*/MIPS 24 μm images from the Far-Infrared Deep Extragalactic Legacy survey (AEGIS; Dickinson & FIDEL Team 2007), S-COSMOS survey (COSMOS; Sanders et al. 2007), GOODS Survey (GOODS-N and GOODS-S; Dickinson et al. 2003), and the *Spitzer* UKIDSS Ultra Deep Survey⁷(UDS; PI:Dunlop). We use a high-resolution $J_{F125W} + H_{F140W} + H_{F160W}$ detection image to model blended sources in the lower resolution MIPS/24 μm image, “cleaning” all galaxies of the contaminating flux of neighboring sources (Section 3, Whitaker et al. 2014). Although UV/optical emission may be spatially offset up to 1” from the IR emission (Chen et al. 2015; Koprowski et al. 2016), this is well within the 6” MIPS/24 μm beam. The galaxy samples for four redshift intervals ($\bar{z} = 0.75, 1.25, 1.75, 2.25$, with $\Delta z = 0.5$), are sub-divided into bins of stellar mass with 0.2 dex width. The number of galaxies within a bin ranges from 7 upwards to 2498 galaxies, with an average value of 652 ± 81 galaxies. Unsurprisingly, the two bins with less than 20 galaxies represent the most massive galaxies ($\log(M_*/M_\odot) = 11.5$) at the highest redshifts ($z > 1.5$). 24 μm flux densities are converted to total IR luminosity, $L_{\text{IR}} \equiv L(8\text{--}1000\mu\text{m})$, based on a single log average of the Dale & Helou (2002, hereafter DH02) templates. We explore this assumption in greater detail in Appendix A. We convert L_{IR} to SFR_{IR} by multiplying by $1.09 \times 10^{-10} M_\odot \text{ yr}^{-1} L_\odot^{-1}$ (Kennicutt 1998a), which assumes a Chabrier (2003) IMF. When considering only the sample above the SFR completeness limits, we confirm that the median stacked SFR_{IR} robustly probes the peak of the individual log-normal distributions within 0.05 dex (Rodighiero et al. 2011). Although the MIPS/24 μm IR SFRs are generally robust for star-forming galaxies at these redshifts in aggregate (e.g., Wuyts et al. 2011; Utomo et al. 2014), we compare the high-redshift results to *Herschel* and SCUBA-2 stacks from the literature in Section 3.

SFR_{UV} is derived from rest-frame UV luminosities based on Bell et al. (2005). The total integrated 1216–3000 \AA UV luminosity is measured from the 2800 \AA rest-frame luminosity multiplied by a factor of 1.5 to account for the UV spectral shape ($L_{\text{UV}} = 1.5L_{2800}$). We adopt the L_{2800} in lieu of 1600 \AA to ensure that the UV continuum is sampled by at least two photometric bands for all galaxies. L_{2800} is determined from the best-fit template using the same methodology as the rest-frame colors (Brammer et al. 2011). To derive the SFR_{UV} , Bell et al. (2005) multiply L_{UV} by both $1.09 \times 10^{-10} M_\odot \text{ yr}^{-1} L_\odot^{-1}$ and a factor of 2.2 that accounts for the unobscured starlight emitted shortward of 1216 \AA and longward of 3000 \AA .

⁷ <http://irsa.ipac.caltech.edu/data/SPITZER/SpUDS/>

Another popular alternative conversion to total SFR is presented in Murphy et al. (2011). This conversion is not only different in the absolute calibration, but also in the relative amount of star formation attributed to the obscured and unobscured phases. Although we adopt the aforementioned SFR calibration to remain consistent with our previous work, we consider in Section 3.1 how this alternative calibration would systematically change the observed correlations.

3. RESULTS

3.1. How does the fraction of obscured star formation depend on stellar mass?

In Figure 1, we present the median relation between $\text{SFR}_{\text{UV+IR}}$ and M_* from $z=0.5$ out to $z=2.5$ from Whitaker et al. (2014). As described in Whitaker et al. (2014), the error bars for L_{IR} are derived from a Monte Carlo bootstrap analysis of the $24\mu\text{m}$ stacks for each stellar mass bin, and added in quadrature to the 1σ scatter in the L_{UV} distributions. We break down the total SFR into the respective unobscured (UV; blue triangles) and obscured (IR; red circles) components. The high transparency symbols signify SFR_{IR} below the 3σ $24\mu\text{m}$ limit, whereas more opaque symbols are above this limit. While we adopt the stacked SFR_{IR} values for all bins, we note that the stacks are in agreement with the detections above the 3σ $24\mu\text{m}$ limits. At all redshifts considered, $>50\%$ of the star formation is obscured for galaxies more massive than $\log(M_*/M_\odot)=9.4$. SFR_{UV} is relatively flat with increasing M_* at each epoch, whereas star forma-

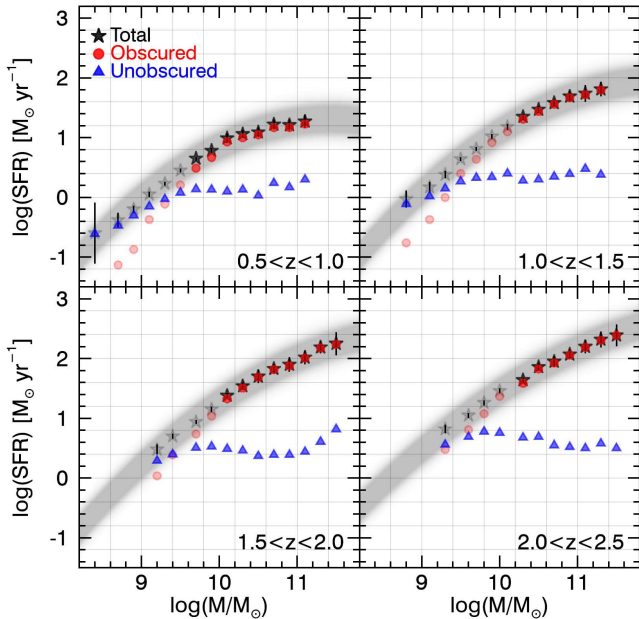


FIG. 1.— The relation between total SFR and M_* (stars) is broken down into the respective unobscured (triangles) and obscured (circles) components. The grey band with Gaussian shading corresponds to the typical 0.3 dex width of the observed relation (e.g. Whitaker et al. 2012b; Speagle et al. 2014). The transparent points signify where SFR_{IR} (and consequently $\text{SFR}_{\text{total}}$) extend below the 3σ limit for individual detections in the $24\mu\text{m}$ imaging; stacking to derive SFR_{IR} is necessary in this regime. Above $\log(M_*/M_\odot)=9.4$ at all redshift epochs between $z=0.5$ and $z=2.5$, the majority of star formation is obscured. Conversely, at lower M_* , star formation is unobscured on average.

TABLE 1
LOGISTIC GROWTH FUNCTION: f_{obscured} VS. $\log(M_*/M_\odot)$

	a	b
Standard Calibration	$(1.96 \pm 0.14) \times 10^9$	-2.277 ± 0.007
Murphy et al. (2011)	$(1.09 \pm 0.09) \times 10^9$	-2.284 ± 0.009

Notes. Logistic growth function coefficients parameterizing the evolution of $f_{\text{obscured}}-\log(M_*/M_\odot)$ using Equation 1. “Standard calibration” corresponds to the adopted luminosity to SFR conversions described herein (solid line, Figure 2); alternative Murphy et al. (2011) conversion also parameterized (dashed line, Figure 2).

tion is increasingly obscured as galaxies gain more stellar mass. This figure demonstrates the importance of using the appropriate SFR diagnostics depending on the M_* regime being considered; it is critical to obtain IR observations to measure robust SFRs for massive galaxies, whereas rest-UV observations will be more important at $\log(M_*/M_\odot) \lesssim 9$.

We observe a remarkably tight correlation between the median obscured star formation fraction ($f_{\text{obscured}} \equiv \widetilde{\text{SFR}}_{\text{IR}} / (\widetilde{\text{SFR}}_{\text{UV}} + \widetilde{\text{SFR}}_{\text{IR}})$) and M_* , generally showing little redshift evolution between $z=0.5$ and $z=2.5$ (Figure 2). Here, we use the error analysis presented in Figure 1 in conjunction with the number of galaxies within a particular bin to derive the error in the mean. The best-fit relation is defined by a logistic growth function:

$$f_{\text{obscured}} = \frac{1}{1 + ae^{b \log(M_*/M_\odot)}}. \quad (1)$$

The greyscale in the left panel of Figure 2 shows the contours of the individual 3D-HST detections relative to the completeness limits at each redshift epoch (thin solid lines). Owing to the extremely deep optical CANDELS/3D-HST photometry, the limiting factor for individual SFRs is the *Spitzer*/MIPS $24\mu\text{m}$ depth. We convert 3σ $24\mu\text{m}$ limits into the limiting SFR_{IR} for each redshift interval (see Figure 2 in Whitaker et al. 2014). When combined with the SFR_{UV} in the 95th percentile for a given M_* and redshift bin, this yields an effective completeness limit. The shape of the completeness curves therefore depends on both the redshift evolution in the distribution of SFR_{UV} and the limiting SFR_{IR} . The 95th percentile is chosen to avoid extreme outliers in SFR_{UV} , while probing the minimum obscuration fraction for a given SFR_{IR} limit.

The scarcity of individual detections near the completeness limits for massive galaxies indicates that they are preferentially highly dust obscured; there is a dearth of massive galaxies that are relatively unobscured. Galaxies are on average $>95\%$ obscured at and above the knee of the mass function (e.g., $\log(M_*/M_\odot)=10.8-11$, Muzzin et al. 2013), and $>70\%$ obscured 1 dex below the characteristic mass (see also Dunlop et al. 2017). While the majority of star formation in the median low-mass galaxy will be observable in the rest-UV, there exists a population of highly obscured low-mass galaxies at $z > 1$ (e.g., Pope et al. 2017). The individual greyscale 3D-HST distribution relative to the median stacked values suggests a large scatter in the amount of obscuration in

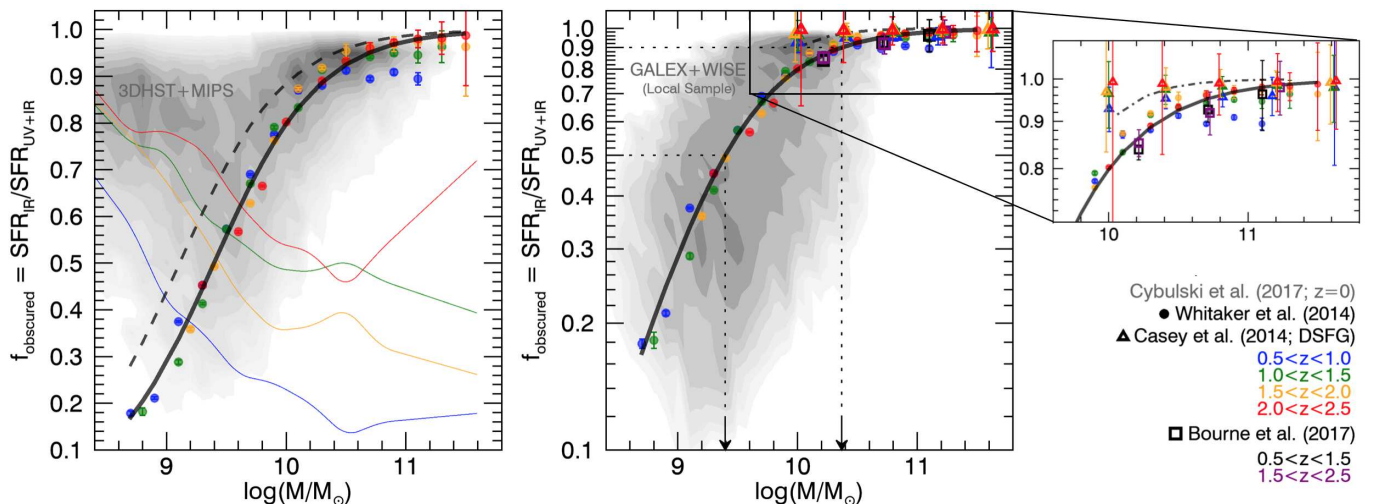


FIG. 2.— The fraction of obscured star formation relative to total derived from median stacks is a strong function of M_* and does not evolve strongly out to $z=2.5$. (Left) Linear y-axis version, including greyscale contours of the individual 3D-HST measurements in addition to the median stacks (circles) from Whitaker et al. (2014). The dashed line is the average relation when using the Murphy et al. (2011) SFR calibrations. The thin lines represent the completeness limits of the $24\mu\text{m}$ imaging. (Right) Logarithmic y-axis version, comparing to a local SDSS sample based on GALEX/WISE photometry at $0.02 < z < 0.05$ in greyscale (Cybulski et al. in prep). We additionally compare to $450\mu\text{m}$ and $850\mu\text{m}$ SCUBA-2 stacks of a mass-selected sample from Bourne et al. (2017), finding excellent agreement at the massive end (squares). The *Herschel* imaging from Casey et al. (2014b) agrees at the massive end down to the limits of the FIR-selected sample of star-forming galaxies (triangles). The dot-dash line represents the implied ratio based on UV light attenuation measurements by Pannella et al. (2009).

galaxies with $\log(M_*/M_\odot) < 9.5$ at $0.5 < z < 2.5$.

Next, we compare with results at $z \sim 0$ (Figure 2, right). The greyscale in the right panel represents 22,481 star-forming galaxies selected at $0.02 < z < 0.05$ from the Sloan Digital Sky Survey DR12 (SDSS; Alam et al. 2015). The SFRs for this local comparison sample are measured from GALEX and WISE/ $22\mu\text{m}$ photometry (see Cybulski et al. in prep for the details). The SDSS mass completeness sets in at much higher masses ($\log(M/M_\odot) \sim 10$) than for 3D-HST. Close to these limits, the data also become limited by the depth of the GALEX and WISE all-sky (but relatively shallow) photometry. We require that the FUV GALEX exposure time is > 100 seconds, resulting in $> 80\%$ completeness across the redshift range. Quiescent galaxies are excluded from this sample on the basis of the specific SFR (SFR/M_*) bimodality, consistent with the 3D-HST UVJ-selection, where we identify and remove galaxies with $\log(\text{sSFR}) < -11$ yr^{-1} . To test how sensitive the resulting SDSS distribution is to this assumption, we conservatively raise and lower this limit in $\log(\text{sSFR})$ by 0.5 dex. Lowering the cut to $\log(\text{sSFR}) = -11.5$ yr^{-1} intersects the peak of the quiescent distribution, whereas raising it to $\log(\text{sSFR}) = -10.5$ yr^{-1} corresponds roughly to the 1σ lower envelope of the star-forming galaxy distribution. We find that the results are not sensitive to our definition of quiescence in the SDSS sample, with the median of the distribution changing only weakly ($\Delta \bar{f}_{\text{observed}} < 0.04$) for a correspondingly large change in the $\log(\text{sSFR})$ limit.

The mode of the SDSS distribution in Figure 2 (right) tracks the higher redshift data well, but with a broader distribution. In Figure 2, there appears to be a dearth of highly obscured low-mass galaxies at $z \sim 0$. We forgo interpretation of the individual distributions at the lowest M_* due to complications by the incompleteness limits of both data sets. For obscuration fractions to the left of the dotted lines, SFR completeness effects will become

important.

We can illuminate the difference in the distributions from $z=2.5$ to $z=0$ for massive galaxies by selecting a bin of $10.6 < \log(M/M_\odot) < 10.8$, where both the SDSS and 3D-HST samples are complete down to low levels of obscured star formation (Figure 3). We find that the distribution at $z=0$ monotonically increases towards a maximum value at 100% obscuration. The mode of the distributions (95-100%) remains relatively unchanged out to $z=2.5$, whereas the width narrows. Although we only show one M_* bin here, we find similar trends down to $\log(M/M_\odot) = 10$. When measuring the median of the distributions (arrows), as also done in the stacking analysis, this suggests a decrease (or flattening) in obscuration at low-redshift for the most massive galaxies. This is also seen in the left panel of Figure 2, where there exists a noteworthy deviation from the best-fit relation for the most massive galaxies in the $0.5 < z < 1.0$ ($1.0 < z < 1.5$) redshift bin, with f_{observed} for galaxies with $\log(M_*/M_\odot) = 11$ depressed by 10% (4%) or 0.05 dex (0.02 dex); see also A2). As shown in Kauffmann et al. (2003), the vast majority of the most massive galaxies in SDSS at $z = 0$ are quiescent. This makes it difficult to push our direct comparison of the distributions presented in Figure 3 towards the highest stellar masses, owing to the sharp drop off in the local sample.

The observation that star formation in the most massive galaxies ($\log(M/M_\odot) > 10.6$) at intermediate redshifts is slightly less dust-obscured can also be seen in Figure 5 of Whitaker et al. (2014), who show IRX ($\equiv L_{\text{IR}}/L_{\text{UV}}$) for this same data analysis as a function of stellar mass. This same redshift bin also has a lower IRX- β relation (Figure 6 Whitaker et al. 2014); the results presented in the right panel of Figure A1 that adopt an evolving template conversion for L_{IR} suggest that we are only under-estimating L_{IR} when using the DH02 log-average template for the most IR-luminous galaxies. The

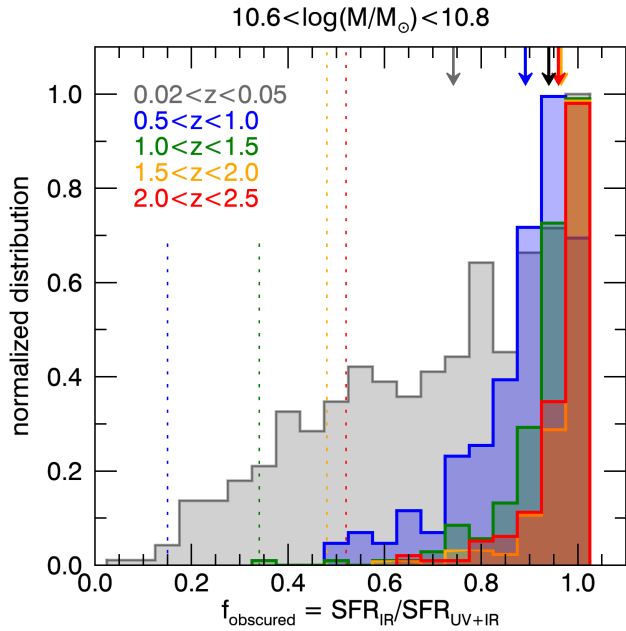


FIG. 3.— Distributions of obscured fraction for individually detected galaxies with $10.6 < \log(M/M_{\odot}) < 10.8$ at $0.02 < z < 0.05$ (SDSS; Cybulski et al. in prep) and $0.5 < z < 2.5$ (3DHST; Whitaker et al. 2014). The arrows mark the distribution medians and the dotted lines (color-coded by redshift) indicate where samples are mass and SFR complete. The black arrow is the best-fit relation from Figure 2. While there is little to no evolution in the mode, the width of the distribution increases towards lower redshifts. This bin is representative of the trends for all M_{\star} where the SDSS and 3D-HST samples are complete.

choice of template therefore will not significantly reduce discrepancies in the IRX- β relation or f_{observed} , as we are probing the median properties of the star-forming galaxy population where the ratio of $L_{\text{IR}}(z)/L_{\text{IR,DH02}}$ is approximately unity. We explore template-dependent effects on L_{IR} in greater detail below and in Appendix A. Both a relative increase in far-UV compared to near-UV attenuation and an increasing stellar population age could result in the shallower IRX- β and $f_{\text{observed}}-\log(M_{\star})$ relations observed (see e.g., Figure 11 in Popping et al. 2017).

3.1.1. The Effects of Alternative SFR_{IR} Methodologies

There exists a range of alternative SFR_{IR} methodologies adopted within the literature. We will explore how our results depend on the assumed calibrations and templates in the following paragraphs. The dashed line in Figure 2 (left) corresponds to the best-fit relation when corrected to the SFR calibrations presented in Equations 3 and 4 of Murphy et al. (2011). Whereas the relative ratio of total star formation originating in IR relative to UV emission is assumed to be $\text{SFR}_{\text{IR}}/\text{SFR}_{\text{UV}}=0.45$ here, Murphy et al. (2011) adopt a higher value of $\text{SFR}_{\text{IR}}/\text{SFR}_{\text{UV}}=0.88$. This results in an overall shift of f_{observed} towards higher fractions of obscured star formation.

Studies show that the MIPS/ $24\mu\text{m}$ photometry is a robust tracer of the average SFR_{IR} out to $z \sim 2-3$ (e.g., Wuyts et al. 2011; Tomczak et al. 2016). However, to rule out potential biases associated with the $24\mu\text{m}$ empirical SFR calibration, we compare our results to several independent studies. Bourne et al. (2017) present

a stacking analysis based on the ultra-deep $450\mu\text{m}$ and $850\mu\text{m}$ over 230 arcmin^2 from the SCUBA-2 Cosmology Legacy Survey in the AEGIS, COSMOS and UDS fields, together with $100-250\mu\text{m}$ imaging from *Herschel*. They adopt a similar deblending approach for the longer wavelength data that relies on the deep photometric catalogs from CANDELS/3D-HST. We adopt a correction to the stellar masses presented in Bourne et al. (2017) of -0.03 dex to convert from Kroupa to Chabrier IMF, following Zahid et al. (2012). We further correct their adopted luminosity to SFR conversion of Murphy et al. (2011) to that used in the present analysis. The utility of the deep MIPS/ $24\mu\text{m}$ photometry is evident when considering the M_{\star} limits achievable with their data analysis. Though the average trends are in excellent agreement with our results, Bourne et al. (2017) are only probing the most massive, obscured galaxies just shy of the M_{\star} regime where the trend sharply falls. They push below the standard confusion limit, but the data is not able to probe the full dynamic range in M_{\star} . When adopting a UV-selected sample, the data presented in Figure 3 of Heinis et al. (2014) is also consistent with no redshift evolution in f_{observed} from $z \sim 4$ to $z \sim 1.5$.

We have also compared to a subset of the *Herschel*-selected sample of dusty star-forming galaxies (DSFG) in the COSMOS field at $0.5 < z < 2.5$ presented in Casey et al. (2014b). As this sample requires direct sub-mm detections, it will be inherently biased towards high fractions of obscured star formation, although the points are consistent within the errors.

Next, we compare our results to Equation 7 in Béthermin et al. (2012); this equation is the $\text{SFR}_{\text{IR}}/\text{SFR}_{\text{UV}}$ ratio based on the UV light attenuation measured in Pannella et al. (2009). Pannella et al. (2009) derived the UV and 1.4 GHz (which is assumed to be a proxy for IR) SFRs of a K-selected BzK sample in the COSMOS field, adopting photometric redshifts at $1 < z < 3$ for $\log(M_{\star}/M_{\odot}) > 10$. We correct the stellar masses from the assumed Salpeter IMF to Chabrier IMF using the conversion of -0.24 dex in Zahid et al. (2012). We convert this equation to the $\text{SFR}_{\text{IR}}/\text{SFR}_{\text{UV+IR}}$ ratio and include this relation in the left panel of Figure 2 for the stellar mass regime considered in Pannella et al. (dot-dash line). It is difficult to differentiate between the effects of sample selection (mass-selected vs. the BzK color-selection), data quality (grism vs. photometric redshifts), and SFR indicators ($24\mu\text{m}$ vs. *Herschel*). Despite these limitations, our result that f_{observed} does not evolve with redshift agrees with the assumptions made in Béthermin et al. (2012) based on data from Pannella et al. (2009).

Finally, we test in greater detail in Appendix A whether our assumption of the single log average of the DH02 templates is driving the results presented in Figure 2. In other words, are we sensitive to the common assumption of a redshift-independent IR spectral energy distribution (SED)? Béthermin et al. (2012) show evidence that the average IR SED of star-forming galaxies evolves with redshift (see also Magdis et al. 2012). In the Bourne et al. (2017) analysis, the models of Béthermin et al. (2012) predict IR luminosities that are a factor of 1.2 higher on average at $2.5 < z < 4$. We present a direct comparison of f_{observed} when measured using the templates of Magdis et al. (2012); Kirkpatrick et al.

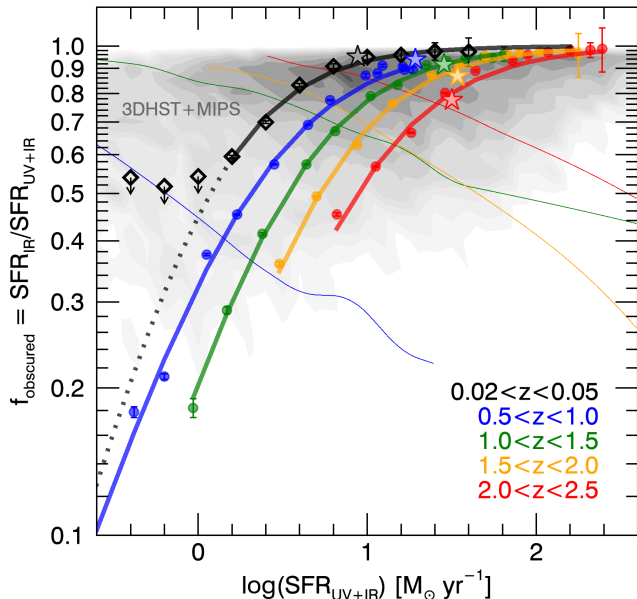


FIG. 4.— The fraction of obscured star formation decreases with increasing redshift at fixed $\text{SFR}_{\text{UV+IR}}$. The median values are derived from GALEX and WISE photometry at $0.02 < z < 0.05$ (black diamonds; Cybulski et al. in prep), and the $0.3\text{--}8\mu\text{m}$ 3D-HST photometry combined with Spitzer/MIPS $24\mu\text{m}$ photometry at $0.5 < z < 2.5$ (circles; Whitaker et al. 2014). The greyscale shows the individual 3D-HST measurements at $0.5 < z < 2.5$, with the thin solid lines representing the respective completeness limits and thick-lines best-fit logistic growth functions. Star symbols represent the inferred evolution of f_{observed} of Milky-Way progenitors across cosmic time.

TABLE 2
LOGISTIC GROWTH FUNCTION: f_{observed} VS.
 $\text{LOG}(\text{SFR}_{\text{UV+IR}})$

	a	b
$0.02 < z < 0.05$	1.234 ± 0.033	-2.858 ± 0.083
$0.5 < z < 1.0$	2.092 ± 0.011	-2.384 ± 0.012
$1.0 < z < 1.5$	3.917 ± 0.049	-2.596 ± 0.017
$1.5 < z < 2.0$	6.806 ± 0.106	-2.673 ± 0.018
$2.0 < z < 2.5$	10.701 ± 0.333	-2.516 ± 0.026

Notes. Logistic growth function coefficients parameterizing the evolution of $f_{\text{observed}} - \text{log}(\text{SFR}_{\text{UV+IR}})$ at different redshift epochs using Equation 2.

(2012, as used in Bethermin et al.) and Kirkpatrick et al. (2015). Although we find a systematic offset towards lower values of f_{observed} at $\text{log}(M_{\star}/M_{\odot}) < 10.5$ than inferred using the DH02 templates, the overall trends remain redshift-independent. Redshift- and L_{IR} -dependent template conversions to bolometric IR luminosity can significantly affect the measured f_{observed} values but not the redshift evolution of the trend itself.

3.2. How does the fraction of obscured star formation depend on total star formation rate?

Next we explore how the fraction of obscured star formation depends on the total $\text{SFR}_{\text{UV+IR}}$. While we saw a marked lack of evolution in the median trends with M_{\star} out to $z=2.5$, we show in Figure 4 that $\text{SFR}_{\text{UV+IR}}$ increases dramatically. However, the overall shape does

not vary strongly. We include the median values from the SDSS $z \sim 0$ sample (Cybulski et al. in prep); this data was reduced and analyzed completely independently, including a different IR calibration (e.g., WISE $22\mu\text{m}$ vs. Spitzer/MIPS $24\mu\text{m}$), yet the evolution is consistent over the full redshift range considered. The best-fit relation for each redshift epoch is defined by a logistic growth function:

$$f_{\text{observed}} = \frac{1}{1 + ae^{b \log(\text{SFR}_{\text{UV+IR}})}}. \quad (2)$$

The strong redshift evolution of the median fraction of obscured star formation as a function of $\text{SFR}_{\text{UV+IR}}$ can be understood generally by the increasing normalization of the star formation sequence, as the global SFR is increasing towards earlier epochs in the Universe (Madau & Dickinson 2014; Schreiber et al. 2015; Tomczak et al. 2016). If we consider galaxies with the same fraction of obscured star formation, we are effectively considering a fixed median stellar mass according to Figure 2. Indeed, $\text{SFR}_{\text{UV+IR}}$ increases by roughly 0.2 dex per $\Delta z \sim 0.5$ at fixed f_{observed} . For fractions $> 70\%$, the evolution in $\text{SFR}_{\text{UV+IR}}$ isn't as dramatic as the curves saturate at maximal levels of obscuration. If we instead consider the evolution of f_{observed} at fixed SFR, we will no longer be probing similar populations of star-forming galaxies across cosmic time. In this case, galaxies with the same SFR at high redshift have significantly lower f_{observed} than at low redshift. Santini et al. (2014) also measure lower dust mass per unit SFR at higher redshifts, in agreement with the results herein.

How do galaxies evolve in this diagram? In reality, we know that galaxies grow with time and therefore fixing stellar mass doesn't ensure we are tracking similar galaxies across cosmic time. To build some intuition, we can instead select galaxies based on fixed number density and use Equation 1 of van Dokkum et al. (2013) to estimate the redshift evolution of stellar mass for Milky-way progenitors, M_{MW} . When combining $M_{\text{MW}}(z)$ with $f_{\text{observed}}(M_{\star})$ from Equation 1 in this paper, we can predict $f_{\text{observed}}(z)$. By adopting the SFR implied by the $\text{log}(\text{SFR}) - \text{log}(M_{\star})$ relation at a given z (see appendix in Whitaker et al. 2017), we can predict the trajectory of a Milky-Way progenitor in f_{observed} and $\text{log}(\text{SFR})$ (star symbols in Figure 4). In this case, f_{observed} changes more rapidly at higher redshift, increasing by 14% from $z=2.25$ to $z=1.25$ (2 Gyr), but only 4% from $z=1.25$ to $z=0$ (8 Gyr).

4. DISCUSSION

In this paper, we demonstrate that at any given fraction of obscured star formation ($f_{\text{observed}} = \text{SFR}_{\text{IR}} / \text{SFR}_{\text{UV+IR}}$), there is little evolution in the median trends with stellar mass over 11 billion years of cosmic time ($z=0$ to $z=2.5$). Interestingly, studies have also found little to no redshift evolution when considering A_{1500} (e.g., Pannella et al. 2009), $A_{\text{H}\alpha}$ (e.g., Sobral et al. 2012), and A_{V} (e.g., Martis et al. 2016) at fixed stellar mass, all quantities parameterizing the amount of dust attenuation. This marks the very epoch over which the SFR density peaks and drops precipitously (Madau & Dickinson 2014), and the metallicities of galaxies of a given mass change by

~ 0.2 – 0.6 dex (e.g., Savaglio et al. 2005; Erb et al. 2006; Kewley & Ellison 2008), with more evolution at the low stellar mass end. Galaxies at higher redshift have lower metallicities and therefore one would expect them to produce less dust. Consequently, if there is a direct scaling between dust mass and L_{IR} , less star formation would be obscured in these galaxies relative to similar masses at low redshift. It is therefore not immediately clear why there is a lack of redshift evolution in f_{obscured} (and dust attenuation) at fixed stellar mass.

The amount of dust in these moderate to massive galaxies ($>10^9 M_{\odot}$) is effectively set by the balance between dust production and destruction. Dust production depends on the growth in the interstellar medium (ISM) via the process of coagulation within molecular clouds. Key additional production channels including supernovae (SNe) and stellar ejecta from stars in the asymptotic giant branch phase of stellar evolution. The ionizing UV and X-ray radiation from massive stars can also easily destroy dust grains, in addition to collisional destruction. While the ISM growth is governed to first order by the volume density of gas and the metallicity, SNe and stellar winds are affected by the SFR volume density (e.g., Popping et al. 2016). Given that the analysis herein is empirically driven in nature, we next explore the how the effects of dust production and destruction could explain the lack of redshift evolution of the $f_{\text{obscured}}\text{-log}(M_{\star})$ relation predominantly in the context of existing observational results.

4.1. Metallicity

First, we will consider the expected effects of metallicity on the amount of dust production through correlations with both dust-to-gas ratio and stellar mass. Observations of local galaxies show that dust-to-gas ratio scales linearly with metallicity above $\sim 0.1 Z_{\odot}$ (e.g., Draine et al. 2007; Leroy et al. 2011; Rémy-Ruyer et al. 2014). This marks a reasonable metallicity threshold for the present study, given that the vast majority of galaxies in our sample should have $Z > 0.1 Z_{\odot}$. If we assume the dust-to-gas ratio does not vary strongly with redshift, as suggested by models (Feldmann 2015; Popping et al. 2016), we can calculate how this quantity scales with stellar mass at various redshift epochs. We describe the details of this analysis in Appendix B. Our compilation of observations of mass-metallicity and dust-to-gas ratio vs. metallicity suggest that the dust-to-gas ratio is a factor of ~ 3 larger at $\log(M/M_{\odot})=11$ as compared to $\log(M/M_{\odot})=9$, with minimal redshift evolution when normalized to the dust-to-gas ratio for the most massive galaxies at a given epoch. In Figure 2, we see a similar relative difference in the fraction of obscured star formation for the same stellar mass range. However, the overall shapes don't quite match in detail; the increase at lower stellar masses is more dramatic for the fraction of obscured star formation relative to change in dust-to-gas ratio, with a 30% larger increase from $\log(M/M_{\odot})=9$ – 10 (see Figure B1).

The tension in the comparison of the fraction of obscured star formation to dust-to-gas ratios as a function of stellar mass will only be amplified when accounting for the fact that gas fractions decrease with stellar mass at a given epoch (e.g. Narayanan et al. 2015; Morokuma-Matsui & Baba 2015; Popping et al.

2015; Scoville et al. 2016; Saintonge et al. 2011, 2016; Tacconi et al. 2013, 2017). Owing to the increased gas fraction of lower mass galaxies relative to more massive galaxies at a given redshift, the relation between dust mass to stellar mass will be shallower than that with dust-to-gas ratio. The total amount of dust (or the column of dust) seen by the UV photons will therefore be higher for lower mass galaxies relative to the dust-to-gas ratio trend, suggesting a higher SFR_{IR} and hence $\text{SFR}_{\text{IR}}/\text{SFR}_{\text{UV+IR}}$. Although this could in principle increase the fraction of obscured star formation at the low mass end, it acts in the wrong direction to alleviate the discrepancies. We therefore find that the drop in f_{obscured} we observe at lower M_{\star} appears to be a stronger function of stellar mass than explainable by the stellar mass dependence of the dust-to-gas ratio.

4.2. Surface Density

Next, we consider the effects of gas surface density on the amount of dust production. An increase in the gas surface density will correlate with an increase in the SFR surface density (Schmidt 1959; Kennicutt 1998b), as well as the column density of dust. Consequently, any redshift evolution in the gas/SFR surface densities would suggest an increase in the level of dust-obscured star formation. We next consider implications from the well-studied average scaling relations of r_e and SFR that comprise the SFR surface density. At fixed stellar mass, observations show that while the average galaxy size (and area) decreases (e.g., van der Wel et al. 2014), the average SFR increases with redshift (e.g., Whitaker et al. 2014). The SFR surface density of galaxies therefore increases on average towards higher redshift (e.g., Wisnioski et al. 2012; Livermore et al. 2015). This is corroborated by a recent archival study by Fujimoto et al. (2017) of ALMA/1mm images, who find that the average size of the gas reservoirs follows a similar redshift evolution to that of the rest-frame optical sizes measured from *HST* imaging. However, the gas size is statistically smaller, suggesting that dust-obscured star formation occurs in compact regions. When combining these various empirical trends with observations of increasing gas fractions (e.g., Tacconi et al. 2017), the data suggest higher gas column densities that produce conditions more suitable to form dust at high redshift, both through star formation and the accretion of metals.

Yet, it may be that the average redshift evolution of the SFR density and galaxy size cancel each other out such that f_{obscured} does not evolve with redshift for a given M_{\star} . We show the normalized average redshift evolution in area (r_e^2) and (s)SFR_{UV+IR} for a narrow range of $9.9 < \log(M_{\star}/M_{\odot}) < 10.1$ in Figure 5 (panel a). The narrow mass bin is intentional such that we select a sample of galaxies that have a similar f_{obscured} on average. We also show the trend of f_{obscured} with redshift in the equivalent stellar mass bin (purple). Note that we are not calculating sSFR/ r_e^2 for any particular individual galaxy but rather using the independently measured trends between SFR and r_e with stellar mass. Given that increased gas and SFR surface densities imply higher dust production at earlier times, it follows that more compact galaxy geometries would decrease dust creation if we want to explain the observed constant median f_{obscured} per M_{\star} with redshift (purple). This is counter-intuitive

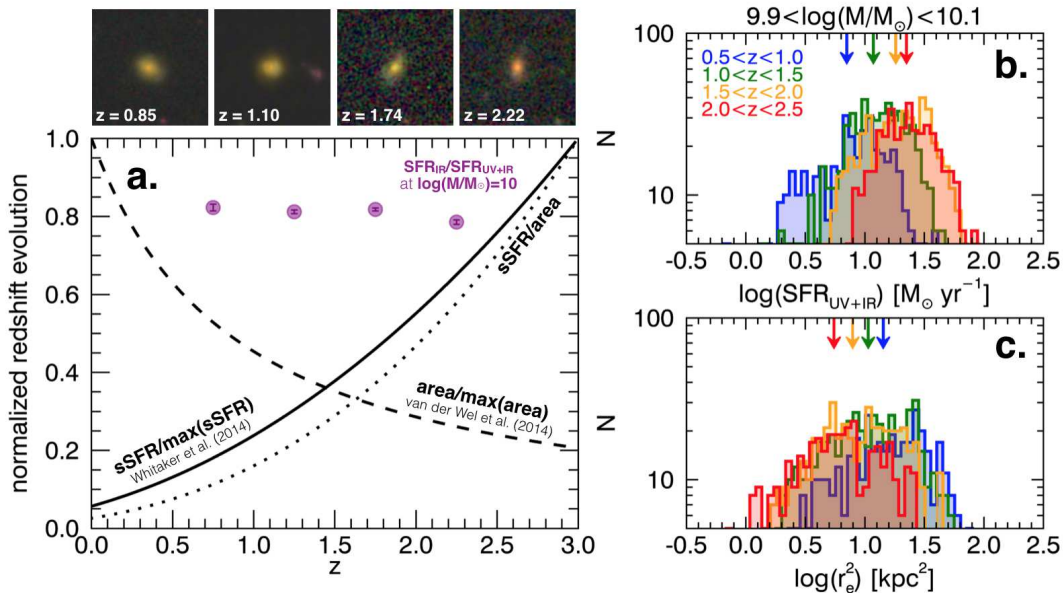


FIG. 5.— Galaxies selected in a narrow range of stellar mass (e.g., $9.9 < \log(M_*/M_\odot) < 10.1$) exhibit similar values of f_{obscured} (e.g., $\sim 80\%$) out to $z=2.5$ (purple circles in panel, taken from Figure 2). Yet the average size and SFR properties are vastly different at different epochs: r_e^2 decreases with increasing redshift (dashed line), while the average sSFR (solid line) and sSFR/area (dotted line) both increase. Given the narrow range in stellar mass, our selection is equivalent to the evolution of SFR and SFR/area (or SFR surface density). The mean of the distributions of $\log(\text{SFR})$ (panel b) and $\log(r_e^2)$ (panel c) demonstrate similar opposing redshift evolution, with arrows marking the median. Even though galaxies exhibit significantly different SFR and size properties at different redshifts on average, as also demonstrated with the example three-color *HST* postage stamps, there is little redshift evolution of their dust properties on a whole.

and poses a challenge to current dust models. Possible explanations can include elevated dust destruction resulting from compact geometries and increased optical thickness. Denser star-forming environments will have an elevated number of supernovae explosions on relatively short timescales, which can either destroy or remove gas and dust in outflows. In the case of more massive galaxies, self-absorption due to the increased optical thickness from higher gas fractions may also play a role.

We see in the right panels of Figure 5 that while the median changes with redshift, the distributions of both sSFR and r_e^2 largely overlap with one another. After removing the well known correlations between stellar mass and SFR and r_e , Whitaker et al. (2017) demonstrate that star-forming galaxies show only a weak dependence of SFR on r_e . As there is little to no correlation between r_e^2 and (s)SFR, the scatter in f_{obscured} for individual galaxies of a similar stellar mass may be quite large in reality. Stacking could hide weaker trends that exist within the scatter, especially if the trends are stronger for some subset of the galaxies, for example. Drawing connections between average galaxy correlations and underlying dust physics is not trivial. Figure 5 serves to caution the reader that intrinsic scatter in the physical properties of galaxies may result in a more complicated redshift evolution of f_{obscured} on a galaxy by galaxy basis.

4.3. Uncertainties in Dust Creation and Destruction

It is worth noting that the obscuration of UV photons is far more complicated than our simplified assumptions regarding the dependence on metallicity or dust column density. Theoretical models must also explicitly take into account how the dust mass, dust-to-gas ratios, and dust column densities translate into the fraction of obscured star formation. It has been shown that the global IR lu-

minosity is not necessarily directly correlated with total dust mass, and consequently SFR_{IR} , as the dust grains in different physical regions are subject to a range of radiation field strengths and hence emit over a range of blackbody temperatures in reality (e.g. Dunne et al. 2000; Draine et al. 2007; Magdis et al. 2012; Kirkpatrick et al. 2017). Moreover, dust geometry can change the extinction law in dense environments around nascent stars, either via dust growth by accretion, grain growth by coagulation where small dust grains stick to larger ones, or grain disruption by shattering where larger grains are shattered by collisions (e.g., Hirashita 2012, 2015). Such processes will change the UV absorption properties of the ISM. And, more generally, empirical studies show that the best-fit attenuation law varies with galaxy type and physical properties (e.g., Wild et al. 2011; Kriek & Conroy 2013; Reddy et al. 2015; Zeimann et al. 2015; Salmon et al. 2016; Battisti et al. 2016). The time evolution of these processes together with the observational uncertainties in the empirical trends quickly results in a complicated picture.

It also may be that global measures of IRX (analogous SFR_{IR} to SFR_{UV}) and $\text{SFR}_{\text{IR}}/\text{SFR}_{\text{UV+IR}}$ are imperfect tracers of true obscuration within galaxies. Are star-forming regions cohabitants with the majority of dust in the ISM? Several case studies find significant offsets between sub-mm and rest-UV/optical emission (e.g., Iono et al. 2006; Chen et al. 2015; Koprowski et al. 2016), suggesting that the bulk of the UV and IR emission may originate from different physical regions in star-forming galaxies at high redshift. If this is a ubiquitous feature of galaxies, the interpretation of a global ratio comparing UV and IR emission becomes muddled. Though beyond the scope of this work, future spatially resolved analyses will illuminate the geometric effects at

play.

Though disentangling the complex interplay between dust geometry and composition with other physical properties of galaxies is beyond the scope of this empirical work, the non-evolution in redshift of the median f_{obscured} as a function of M_{\star} points to very little redshift evolution in the characteristics of dust on a whole. Rigorous theoretical analyses will be required to understand the exact balance between the dust creation and destruction processes mentioned above across time in the context of these empirical results.

5. CONCLUSIONS

In this paper, we explore how the total star formation rate and stellar masses of galaxies depend on the relative amount of obscured star formation. Our main mass-complete galaxy sample is comprised of 39,106 star-forming galaxies at $0.5 < z < 2.5$ (Whitaker et al. 2014), selected from the 3D-HST/CANDELS treasury programs in the five premier extragalactic fields. This deep near-infrared photometry yields mass-complete galaxy samples down to unprecedented limits of $\log(M/M_{\odot}) = 8.7$ (9.3) at $z = 1.0$ ($z = 2.5$). Unobscured star formation rates are measured directly from the 3D-HST photometry, and obscured star formation is quantified based on stacks of deep *Spitzer*/MIPS $24\mu\text{m}$ photometry. We expand the baseline of the analysis by combining this novel data set with a local SDSS sample of 22,481 star-forming galaxies at $0.02 < z < 0.05$, with total star formation rates measured from GALEX and WISE photometry.

The main findings of our analysis are summarized as:

1. We observe a strong dependence of the median fraction of obscured star formation (defined as $f_{\text{obscured}} = \text{SFR}_{\text{IR}} / \text{SFR}_{\text{UV+IR}}$) on stellar mass. This correlation shows remarkably little evolution across the full redshift range explored ($z = 0$ to $z = 2.5$), extending earlier results (e.g., Heinis et al. 2014; Bourne et al. 2017) to lower stellar mass limits.
2. The transition from mostly unobscured to obscured star formation ($f_{\text{obscured}} = 0.5$) occurs at a relatively low stellar mass of $\log(M/M_{\odot}) = 9.4$. Even though the majority of the star formation in galaxies with $\log(M/M_{\odot}) < 9.4$ is radiated in the rest-frame UV, there exists a tail of low-mass extremely obscured star-forming galaxies at $z > 1$. For the most massive galaxies, with $\log(M/M_{\odot}) > 10.5$, $>90\%$ of star formation is obscured at all redshifts.

3. We find that the fraction of star formation obscured by dust, f_{obscured} , at fixed total SFR decreases at higher redshift. As the normalization of the $\log(\text{SFR}) - \log(M_{\star})$ relation is increasing with redshift while $f_{\text{obscured}} - \log(M_{\star})$ is unchanged, the same total SFR probes lower stellar mass limits at higher redshifts.

We explore the implications of these findings in the context of a range of well-studied empirical trends between dust-to-gas ratio, metallicity, gas and SFR surface density, gas fraction and stellar mass. Galaxies at high redshift are observed to have more compact sizes and significantly higher star formation rates, gas fractions, and hence gas and SFR surface densities. The straightforward interpretation is therefore that star formation should be more highly obscured at early times. It is therefore puzzling that we observe no redshift evolution in the median fraction of obscured star formation with stellar mass out to $z = 2.5$. Given the complexity of the various physical processes governing the attenuation of UV photons, including but not limited to dust geometry and composition, key progress can be made in understanding these results with future theoretical models.

We thank the anonymous referee for useful comments and a careful reading of the paper. The authors wish to acknowledge P. van Dokkum, I. Momcheva, R. Skelton, G. Brammer, the 3D-HST team and colleagues for their hard work in releasing public data and catalogs in the 3D-HST fields. KEW is grateful for discussions with N. Katz. KEW gratefully acknowledges support by NASA through Hubble Fellowship grant #HST-HF2-51368 awarded by the Space Telescope Science Institute, which is operated by the Association of Universities for Research in Astronomy, Inc., for NASA, under contract NAS 5-26555. MSY and RC acknowledges support from the NASA ADAP grant NNX14AF80G. CMC thanks the UT Austin College of Natural Science for support. This work is based on observations taken by the 3D-HST Treasury Program (GO 12177 and 12328) with the NASA/ESA HST, which is operated by the Associations of Universities for Research in Astronomy, Inc., under NASA contract NAS5-26555.

APPENDIX

APPENDIX A.

In order to explore the effect of template uncertainties on the calculation of IR SFRs, we compare our data to the template set adopted within Béthermin et al. (2012) and Kirkpatrick et al. (2015, hereafter K15). Béthermin et al. use a redshift-dependent IR SED template set for “typical” star-forming galaxies and starbursts from Magdis et al. (2012, hereafter M12), based on fits of the Draine et al. (2007) models. K15 published empirical composite templates of star-forming galaxies at $0.4 < z < 1.4$ for $L_{\text{IR}} \sim 4 \times 10^{11}$ and $1 \times 10^{12} L_{\odot}$, plus a higher redshift template at $1.4 < z < 2.1$ for $L_{\text{IR}} \sim 1 \times 10^{12} L_{\odot}$. We use the K15 together with the M12 templates for “main sequence” star-forming galaxies at $1.0 < z < 1.3$ and $1.75 < z < 2.25$ to recalculate L_{IR} for all the galaxies in the 3D-HST catalog that have a positive $24\mu\text{m}$ flux densities at the relevant redshifts (Figure A1).

The right panel in Figure A1 shows the ratio of L_{IR} from the K15 and M12 templates to the DH02 template used in Whitaker et al. (2012b, 2014) and this paper, color-coded based on the template adopted. In general, we find that the M12 and K15 templates predict a mild redshift and L_{IR} dependence on the conversion from $24\mu\text{m}$ flux density to bolometric IR luminosity (Figure A1, right panel). The trend is consistent between the K15 and M12 templates, though M12 does not explicitly isolate galaxy samples based on L_{IR} . The dashed lines in the right panel show the

best-fit linear function, which we quantify as a function of redshift and L_{IR} to be:

$$L_{\text{IR}}(z)/L_{\text{IR,DH02}} = -0.35z + 0.65 \times \log(L_{\text{IR}}) - 6.3 \quad (\text{A1})$$

In order to isolate if template-dependent effects are driving the results shown in Figure 2, we correct L_{IR} in the 3D-HST catalogs using the equation above and recalculate $\text{SFR}_{\text{IR}}/\text{SFR}_{\text{UV+IR}}$ vs. $\log(M_{\star})$. To avoid over-interpreting the K15 and M12 templates, we only consider the regime of $\log(M_{\star}/M_{\odot}) > 9.7$, which corresponds to the lower mass limit of galaxies in the M12 sample. Although the K15 sample does not include such low mass galaxies, the results are consistent between the two independent template sets (Right panel, Figure A1). The ratio of the measured values of $f_{\text{observed}} = \text{SFR}_{\text{IR}}/\text{SFR}_{\text{UV+IR}}$ from the redshift- and L_{IR} -dependent relation relative to the original redshift-independent DH02 template decreases from $\sim 30\%$ (0.15 dex) difference at $\log(M_{\star}/M_{\odot}) \sim 10$ to $< 5\%$ (< 0.02 dex) difference at $\log(M_{\star}/M_{\odot}) > 10.5$.

In Figure A2, we compare f_{observed} corrected for the redshift- and L_{IR} -dependence of the templates relative to the original stacks based on the DH02 templates. The middle panel directly compares to the original data, whereas the right panel is comparing the corrected f_{observed} to the redshift-independent best-fit to the original data (shown as the thick black line in left-most panel for reference). The M12 and K15 empirical templates suggest that L_{IR} is over-predicted for lower mass galaxies with $\log(M_{\star}/M_{\odot}) \sim 10$, such that f_{observed} is also overpredicted by as much as 50% (0.3 dex). However, f_{observed} agrees regardless of the template conversion adopted for more massive galaxies above

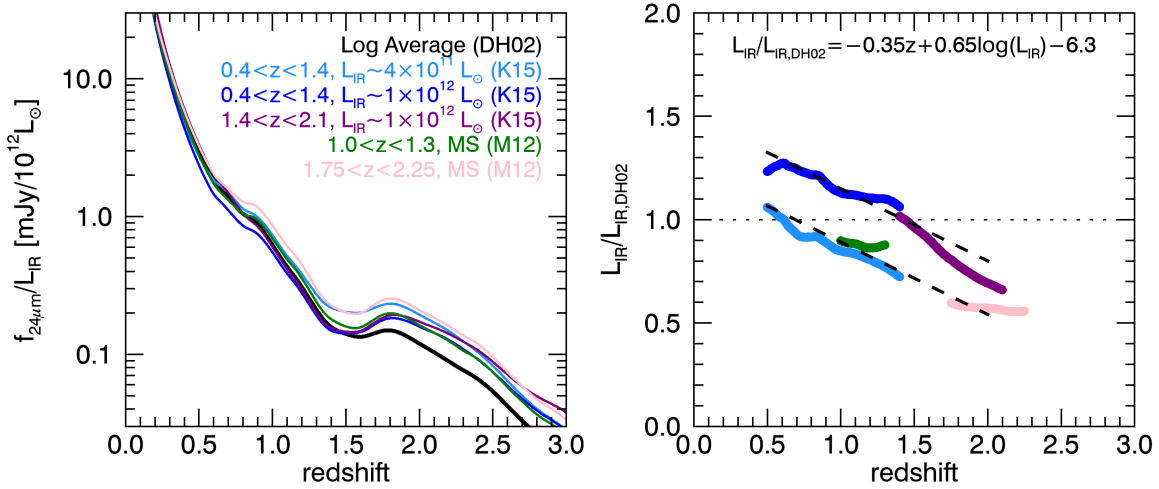


FIG. A1.— (Left) Comparison of different template conversions transforming $24\mu\text{m}$ flux density to L_{IR} relative to the redshift-independent DH02 templates adopted herein. We compare to the empirical templates of Kirkpatrick et al. (2015) (K15) and Magdis et al. (2012) (M12). The K15 templates explore a range of L_{IR} for two redshift intervals, whereas the two M12 templates shown are for typical star-forming galaxies at different redshift epochs. (Right) The resulting L_{IR} from the K15 and M12 templates relative to the DH02 templates mildly evolves with redshift. We parameterize this evolution as a function of redshift and L_{IR} (dashed lines) to test how this affects the obscured SFR presented in this paper.

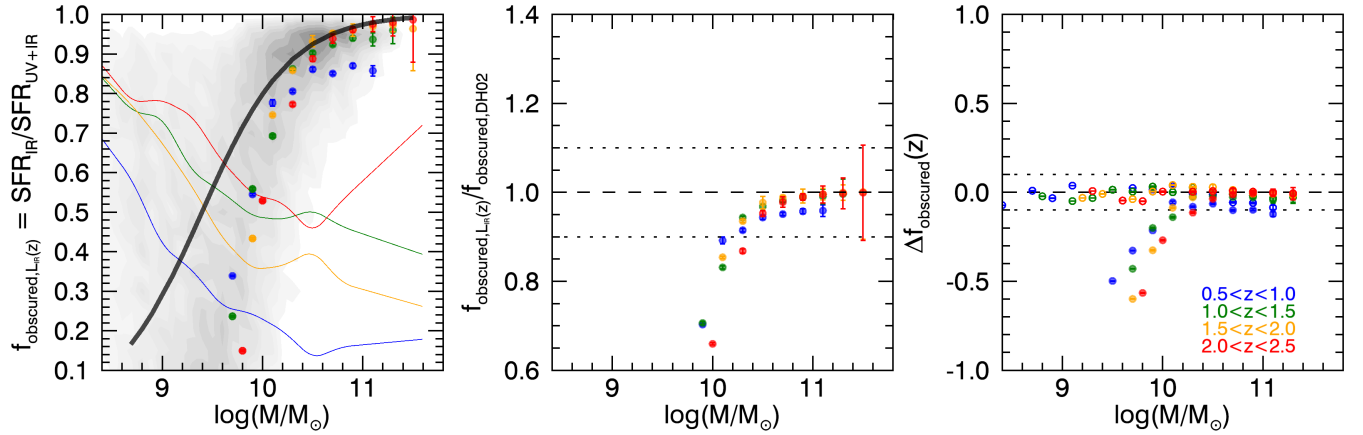


FIG. A2.— (Left) Changing the template conversion of $24\mu\text{m}$ flux density to L_{IR} , using the equation in Figure A1b, changes the overall shape of f_{observed} as a function of stellar mass, but the relation still does not vary strongly with redshift. This is demonstrated in the middle and right panels, where we compare the ratio of the new f_{observed} relative to the original using the DH02 templates (middle panel) and the difference between the new f_{observed} and the best-fit model (right panel). The scatter between the original data and best-fit line (open circles) increases slightly when considering the K15/M12 template conversions (filled circles). The difference due to template conversion is negligible at $\log(M/M_{\odot}) > 10.5$.

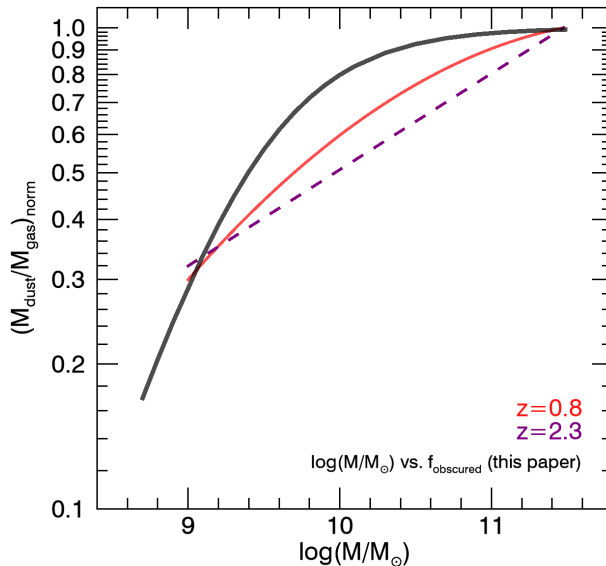


FIG. B1.— The relative change in the ratio of dust-to-gas mass with stellar mass (normalized to unity at $\log(M/M_{\odot})=11.5$) at $z=0.8$ (purple) and $z=2.3$ (red) is similar to that of f_{observed} : Massive galaxies with $\log(M/M_{\odot})=11$ have a factor of three higher dust-to-gas mass and f_{observed} than lower mass galaxies, $\log(M/M_{\odot})=9$. However, the overall shape of the dust-to-gas mass as a function of stellar mass relative to the stellar mass dependence of f_{observed} (black, from Figure 2) is different.

$\log(M_{\star}/M_{\odot}) > 10.5$ within $<5\%$ (0.02 dex). Interestingly, the analysis presented in Wuyts et al. (2011) found that while L_{IR} derived using $24\mu\text{m}$ flux densities with the full DH02 template set is over-predicted for the most massive, higher redshift galaxies ($\log(\text{SFR}) > 2 M_{\odot} \text{ yr}^{-1}$) in our sample by up to ~ 0.5 dex, the systematic offset is much weaker for the log-average of the DH02 templates. We show here that using an evolving template set for the $24\mu\text{m}$ conversion may alleviate any remaining discrepancy.

Despite different trends that emerge when employing a different template conversion from the 24μ flux density to bolometric IR luminosity, the lack of redshift evolution in f_{observed} with stellar mass remains a robust conclusion. Namely, the scatter between f_{observed} for different redshift epochs in the middle and right-most panel of Figure A2 remains small, even when utilizing a redshift dependent conversion.

APPENDIX B.

In order to directly compare the dust-to-gas ratio as a function of stellar mass, we take two well measured correlations: the dust-to-gas ratio as a function of metallicity from Rémy-Ruyer et al. (2014), and mass-metallicity relations that bookend our redshift distribution. We adopt the mass-metallicity relation presented in Zahid et al. (2011) at $z \sim 0.8$ from the AEGIS/DEEP-2 spectroscopic sample, and Steidel et al. (2014) at $z \sim 2.3$ from KBSS-MOSFIRE spectroscopy. The mass-metallicity relation results at $z \sim 2.3$ from the MOSDEF survey (Sanders et al. 2015) are consistent with Steidel et al. (2014) when selecting targets from the mass-complete 3D-HST parent sample. In Figure B1, we normalize the parameterized relation between dust-to-gas ratio and stellar mass at $z=0.8$ (purple) and $z=2.3$ (red) at $\log(M/M_{\odot})=11.5$ to facilitate a direct comparison with the best-fit relation from Figure 2 (black). We explore the relative dependence of dust-to-gas ratio and f_{observed} on stellar mass in the main body of the paper.

REFERENCES

- Alam, S., Albareti, F. D., Allende Prieto, C., et al. 2015, *ApJS*, 219, 12
- Battisti, A. J., Calzetti, D., & Chary, R.-R. 2016, *ApJ*, 818, 13
- Bell, E. F., Papovich, C., Wolf, C., et al. 2005, *ApJ*, 625, 23
- Bertin, E., & Arnouts, S. 1996, *A&AS*, 117, 393
- Béthermin, M., Daddi, E., Magdis, G., et al. 2012, *ApJ*, 757, L23
- Bourne, N., Dunlop, J. S., Merlin, E., et al. 2017, *MNRAS*, 467, 1360
- Brammer, G. B., van Dokkum, P. G., & Coppi, P. 2008, *ApJ*, 686, 1503
- Brammer, G. B., Whitaker, K. E., van Dokkum, P. G., et al. 2011, *ApJ*, 739, 24
- Bruzual, G., & Charlot, S. 2003, *MNRAS*, 344, 1000
- Calzetti, D. 2013, *Star Formation Rate Indicators*, ed. J. Falcón-Barroso & J. H. Knapen, 419
- Calzetti, D., Armus, L., Bohlin, R. C., et al. 2000, *ApJ*, 533, 682
- Casey, C. M., Narayanan, D., & Cooray, A. 2014a, *Phys. Rep.*, 541, 45
- Casey, C. M., Scoville, N. Z., Sanders, D. B., et al. 2014b, *ApJ*, 796, 95
- Chabrier, G. 2003, *PASP*, 115, 763
- Chen, C.-C., Smail, I., Swinbank, A. M., et al. 2015, *ApJ*, 799, 194
- Cortese, L., Boselli, A., Buat, V., et al. 2006, *ApJ*, 637, 242
- Dale, D. A., & Helou, G. 2002, *ApJ*, 576, 159
- Dickinson, M., & FIDEL Team. 2007, in *Bulletin of the American Astronomical Society*, Vol. 39, American Astronomical Society Meeting Abstracts, 822
- Dickinson, M., Papovich, C., Ferguson, H. C., et al. 2003, *ApJ*, 587, 25
- Donley, J. L., Koekemoer, A. M., Brusa, M., et al. 2012, *ApJ*, 748, 142
- Draine, B. T., Dale, D. A., Bendo, G., et al. 2007, *ApJ*, 663, 866
- Dunlop, J. S., McLure, R. J., Biggs, A. D., et al. 2017, *MNRAS*, 466, 861
- Dunne, L., Eales, S., Edmunds, M., et al. 2000, *MNRAS*, 315, 115
- Erb, D. K., Shapley, A. E., Pettini, M., et al. 2006, *ApJ*, 644, 813
- Feldmann, R. 2015, *MNRAS*, 449, 3274
- Fujimoto, S., Ouchi, M., Shibuya, T., et al. 2017, *ArXiv e-prints*
- Grogin, N. A., Kocevski, D. D., Faber, S. M., et al. 2011, *ApJS*, 197, 35

- Heinis, S., Buat, V., Béthermin, M., et al. 2014, *MNRAS*, 437, 1268
- Hirashita, H. 2012, *MNRAS*, 422, 1263
- , 2015, *MNRAS*, 447, 2937
- Iono, D., Peck, A. B., Pope, A., et al. 2006, *ApJ*, 640, L1
- Kauffmann, G., Heckman, T. M., White, S. D. M., et al. 2003, *MNRAS*, 341, 33
- Kennicutt, Jr., R. C. 1998a, *ARA&A*, 36, 189
- , 1998b, *ApJ*, 498, 541
- Kennicutt, Jr., R. C., Hao, C.-N., Calzetti, D., et al. 2009, *ApJ*, 703, 1672
- Kewley, L. J., & Ellison, S. L. 2008, *ApJ*, 681, 1183
- Kirkpatrick, A., Pope, A., Alexander, D. M., et al. 2012, *ApJ*, 759, 139
- Kirkpatrick, A., Pope, A., Sajina, A., et al. 2017, *ApJ*, 843, 71
- , 2015, *ApJ*, 814, 9
- Koprowski, M. P., Coppin, K. E. K., Geach, J. E., et al. 2016, *ApJ*, 828, L21
- Kriek, M., & Conroy, C. 2013, *ApJ*, 775, L16
- Kriek, M., van Dokkum, P. G., Franx, M., et al. 2009, *ApJ*, 705, L71
- Leroy, A. K., Bolatto, A., Gordon, K., et al. 2011, *ApJ*, 737, 12
- Livermore, R. C., Jones, T. A., Richard, J., et al. 2015, *MNRAS*, 450, 1812
- Madau, P., & Dickinson, M. 2014, *ARA&A*, 52, 415
- Magdis, G. E., Daddi, E., Béthermin, M., et al. 2012, *ApJ*, 760, 6
- Magnelli, B., Elbaz, D., Chary, R. R., et al. 2009, *A&A*, 496, 57
- Martis, N. S., Marchesini, D., Brammer, G. B., et al. 2016, *ApJ*, 827, L25
- Meurer, G. R., Heckman, T. M., & Calzetti, D. 1999, *ApJ*, 521, 64
- Momcheva, I. G., Brammer, G. B., van Dokkum, P. G., et al. 2016, *ApJS*, 225, 27
- Morokuma-Matsui, K., & Baba, J. 2015, *MNRAS*, 454, 3792
- Muñoz-Mateos, J. C., Gil de Paz, A., Boissier, S., et al. 2009, *ApJ*, 701, 1965
- Murphy, E. J., Condon, J. J., Schinnerer, E., et al. 2011, *ApJ*, 737, 67
- Muzzin, A., Marchesini, D., Stefanon, M., et al. 2013, *ApJS*, 206, 8
- Narayanan, D., Turk, M., Feldmann, R., et al. 2015, *Nature*, 525, 496
- Pannella, M., Carilli, C. L., Daddi, E., et al. 2009, *ApJ*, 698, L116
- Pope, A., Montaña, A., Battisti, A., et al. 2017, *ApJ*, 838, 137
- Popping, G., Caputi, K. I., Trager, S. C., et al. 2015, *MNRAS*, 454, 2258
- Popping, G., Puglisi, A., & Norman, C. A. 2017, *ArXiv e-prints*
- Popping, G., Somerville, R. S., & Galametz, M. 2016, *ArXiv e-prints*
- Reddy, N. A., Kriek, M., Shapley, A. E., et al. 2015, *ApJ*, 806, 259
- Rémy-Ruyer, A., Madden, S. C., Galliano, F., et al. 2014, *A&A*, 563, A31
- Rodighiero, G., Daddi, E., Baronchelli, I., et al. 2011, *ApJ*, 739, L40
- Saintonge, A., Catinella, B., Cortese, L., et al. 2016, *MNRAS*, 462, 1749
- Saintonge, A., Kauffmann, G., Kramer, C., et al. 2011, *MNRAS*, 415, 32
- Salmon, B., Papovich, C., Long, J., et al. 2016, *ApJ*, 827, 20
- Sanders, D. B., Salvato, M., Aussel, H., et al. 2007, *ApJS*, 172, 86
- Sanders, R. L., Shapley, A. E., Kriek, M., et al. 2015, *ApJ*, 799, 138
- Santini, P., Maiolino, R., Magnelli, B., et al. 2014, *A&A*, 562, A30
- Savaglio, S., Glazebrook, K., Le Borgne, D., et al. 2005, *ApJ*, 635, 260
- Schmidt, M. 1959, *ApJ*, 129, 243
- Schreiber, C., Pannella, M., Elbaz, D., et al. 2015, *A&A*, 575, A74
- Scoville, N., Sheth, K., Aussel, H., et al. 2016, *ApJ*, 820, 83
- Seibert, M., Martin, D. C., Heckman, T. M., et al. 2005, *ApJ*, 619, L55
- Skelton, R. E., Whitaker, K. E., Momcheva, I. G., et al. 2014, *ApJS*, 214, 24
- Sobral, D., Best, P. N., Matsuda, Y., et al. 2012, *MNRAS*, 420, 1926
- Speagle, J. S., Steinhardt, C. L., Capak, P. L., et al. 2014, *ArXiv e-prints*
- Steidel, C. C., Rudie, G. C., Strom, A. L., et al. 2014, *ArXiv e-prints*
- Tacconi, L. J., Genzel, R., Saintonge, A., et al. 2017, *ArXiv e-prints*
- Tacconi, L. J., Neri, R., Genzel, R., et al. 2013, *ApJ*, 768, 74
- Tal, T., Dekel, A., Oesch, P., et al. 2014, *ArXiv e-prints*
- Tomczak, A. R., Quadri, R. F., Tran, K.-V. H., et al. 2016, *ApJ*, 817, 118
- Utomo, D., Kriek, M., Labbé, I., et al. 2014, *ApJ*, 783, L30
- van der Wel, A., Franx, M., van Dokkum, P. G., et al. 2014, *ApJ*, 788, 28
- van Dokkum, P. G., Leja, J., Nelson, E. J., et al. 2013, *ApJ*, 771, L35
- Viero, M. P., Moncelsi, L., Quadri, R. F., et al. 2013, *ApJ*, 779, 32
- Whitaker, K. E., Bezanson, R., van Dokkum, P. G., et al. 2017, *ApJ*, 838, 19
- Whitaker, K. E., Franx, M., Leja, J., et al. 2014, *ApJ*, 795, 104
- Whitaker, K. E., Kriek, M., van Dokkum, P. G., et al. 2012a, *ApJ*, 745, 179
- Whitaker, K. E., van Dokkum, P. G., Brammer, G., et al. 2012b, *ApJ*, 754, L29
- Wild, V., Charlot, S., Brinchmann, J., et al. 2011, *MNRAS*, 417, 1760
- Wisnioski, E., Glazebrook, K., Blake, C., et al. 2012, *MNRAS*, 422, 3339
- Wuyts, S., Förster Schreiber, N. M., Lutz, D., et al. 2011, *ApJ*, 738, 106
- Zahid, H. J., Dima, G. I., Kewley, L. J., et al. 2012, *ApJ*, 757, 54
- Zahid, H. J., Kewley, L. J., & Bresolin, F. 2011, *ApJ*, 730, 137
- Zeimann, G. R., Ciardullo, R., Gronwall, C., et al. 2015, *ApJ*, 814, 162